Chapter 4

Superlubricity of nanohybrid of polyaniline functionalized reduced graphene oxide with yttrium and vanadium co-doped zinc oxide nanoparticles

Chapter 4

Graphene is considered a single-atom-thick two-dimensional array of sp^2-hybridized carbon atoms in a compact honeycomb crystal lattice [Paul et al. (2019), Kuila et al. (2012)]. It has acquired felicitous status in the scientific world due to its distinctive characteristics, such as low thermal expansion coefficient but exceptionally high mechanical flexibility, optical transparency, thermal and electrical conductivity [Verma et al. (2019), Gupta et al. (2016), Wang et al. (2020), Kuila et al. (2012)]. The lubricity of graphene sheets has been very well recognized due to the existing weak van der Waals forces between adjacent layers [Gupta et al. (2016), Wang et al. (2020)]. The chemical inertness of graphene results in its feeble adherence to the surface. Owing to its high surface area and surface energy, graphene tends to agglomerate and go back to graphitic form [Ota et al. (2015)]. Consequently, its dispersion in different media is reduced [Kuila et al. (2012)]. Chemical functionalization of graphene is a remedial measure to curb its agglomeration, restacking, and promote dispersion [Chouhan et al. (2020), Kuila et al. (2012), Paul et al. (2019)]. It also enhances the adhesion to the interacting surface. Surface modification of graphene oxide can be achieved by covalent and non-covalent pathways. For a covalent modification, a chemical attack is conducted at selective sites on graphene oxide. It may lead to nucleophilic/electrophilic substitution, condensation, or addition reactions depending on the choice of the reagent [Mungse et al. (2019), Kuila et al. (2012), Georgakilas et al. (2012), Zhang et al. (2017), Tang et al. (2018), Paul et al. (2019), Gusain et al. (2016), Mungse et al. (2014), Chouhan et al. (2018)]. Weaker interactions like electrostatic, π-π, or van der Waals forces are introduced when a non-covalent modification is performed [Kuila et al. (2012)].

Nanoparticles of metals such as Ni [Chou et al. (2010)], Cu [Guo et al. (2020), Chou et al. (2011), Kumara et al. (2019)], Ag [Ma et al. (2009), Kumara et al. (2017),], Pd [Kumara et al. (2018)], Zhang et al. (2014)] and metal salts such as oxides; ZrO_2 [Rylski et al. (2020), Liu et al. (2018), Philip et al. (2019), Verma et al. (2020a)], ZnO [Battez et al. (2008), Kalyani et al. (2016)], CeO_2 [Shen et al. (2016)], sulfides; MoS_2 [Xie et al. (2016), Koshy et al. (2015), Ratoi et al. (2014)]], Ag_2S [Ma et al. (2019), Xu et al. (2019)], CuS [Kang et al. (2008)], halides; LaF_3 [Li et al. (2014), Zhou et al. (2001), Li et al. (2014)] have been extensively investigated as components of nano lubricants [Singh et al. (2020), Uflyand et al. (2019)]. Their composites with graphene, such as copper [Ali et al. (2019], silver [Xu et al. (2018), Meng et al. (2016)], Mn_3O_4 [Zhao et al. (2019)], ceria [Bai et al. (2014)], zirconia [Zhou et al. (2015)], boron nitride [Liu et al. (2018)] and WS_2 [Zheng et al. (2017)], are well documented in the literature for enhanced tribological performance. Titanium dioxide reinforced boron nitrogen co-doped graphene nanocomposite was reported from our laboratory for excellent tribological activity [Jaiswal et al. (2016)]. Some reports are available in the literature where the activity of doped nanoparticles is enhanced significantly after doping with some other ion [Jaiswal et al. (2014), Kalyani et al. (2016), Li et al. (2017)]. Accordingly, magnesium doped zinc oxide nanoparticles (ZMO) and their nanohybrid with reduced graphene oxide (ZMO-rGO) were prepared in our laboratory. We have found that the tribological activity of ZMO/rGO was much better than that of ZnO/rGO [Verma et al. (2019)]. The ternary composites, (La-Y_2O_3)-MoS_2-(M-rGO) (M=methionine), and CuPc-(ADB-rGO) [Pc = phthalocyanine, ADB = 2-aminoethyl diphenyl borate] have also been

reported by our group for remarkable tribological activity [Shukla et al. (2020), Verma et al. (2020b)].

Motivated from our previous work, it appeared to us engrossing to dope zinc oxide nanoparticles with two different ions in different oxidation states expecting more defects but retaining its wurtzite structure and see the effect on tribological activity. Yttrium doped nanocrystalline zinc oxide and vanadium doped ZnO nanoparticles have exhibited photocatalytic activity in methylene blue degradation [Sanoop et al. (2016), Slama et al. (2011)]. Yttrium and vanadium co-doped zinc oxide photocatalyst has been used to enhance dye-sensitized visible light photochemical activity [Alam et al. (2017)]. Since yttrium oxide [Shukla et al. (2020)] and vanadium oxide [(Dai et al. (2017)] both are known to show tribological properties, zinc oxide was doped with yttrium (1%) and vanadium (3%). Doping was performed up to a total of 4% to avoid any phase changes in the zinc oxide crystal lattice [Mamouni et al. (2018), Joshi et al.(2014)].

Furthermore, graphene-based polymer nanocomposites have been noted for enhanced mechanical, thermal, and electrical properties [Kuila et al. (2012), Georgakilas et al. (2012), Haruna et al. (2019)]. Graphene nanosheet-wrapped polyaniline rectangular-like nanotubes have found application as supercapacitor [Qin et al. (2017)]. Graphene/ polyaniline composite film synthesized electrochemically has been applied as biosensors due to its biocompatibility [Kumar et al. (2012)]. Similarly, graphene/ graphene oxide-polyaniline hybrids have found significance in bio-sciences [Wang et al. (2019)]. Thermoelectric

applications of reduced graphene oxide-polyaniline composites have been reported [Mitra et al. (2015)]. Polyaniline-modified graphene oxide epoxy nanocomposite film has been investigated for UV blocking/ anti-oxidant/ anti-corrosion capabilities [Amrollahi et al. (2019)]. Polyaniline/graphene composites have been applied in waterborne polyurethane anticorrosive coatings [Yuan et al. (2016)]. Polyaniline doped grease has shown corrosion resistance and tribological characteristics [Cao et al. (2017)]. Polyaniline/reduced graphene oxide/Fe_3O_4 nanocomposite has been studied to remove mercuric ions in water [Li et al. (2015)]. Recently, polyaniline functionalized graphene oxide has been shown to possess excellent tribological activity [Liu et al. (2018)]. The present investigation, therefore, includes the non-covalent functionalization of reduced graphene oxide with polyaniline (PANI-rGO). The nanoparticles of yttrium/vanadium- doped zinc oxide and yttrium - vanadium co-doped zinc oxide nanoparticles have been prepared by the auto combustion method. Further, the as-prepared doped nanoparticles have been used to functionalize PANI-rGO non-covalently to yield Y-V-ZnO/PANI-rGO, and its tribological activity has been evaluated in paraffin oil using a four-ball tester.

4.1. Materials and Methods

4.1.1. Chemicals

Zinc nitrate hexahydrate [$Zn(NO_3)_2.6H_2O$], yttrium nitrate hexahydrate [$Y(NO_3)_3.6H_2O$], ammonium vanadate (NH_4VO_3), citric acid, hydrochloric acid (HCl), aniline, and ammonium peroxide sulfate were procured from Merck.

4.1.2. Synthesis of Additives

4.1.2.1. Synthesis of Nanoparticles

Synthesis of Y-ZnO, V-ZnO, and Y-V-ZnO nanoparticles was achieved by the auto-combustion method [Verma et al. (2019), Liu et al. (2015)]. For the preparation of Y-ZnO, zinc nitrate hexahydrate $Zn(NO_3)_2.6H_2O$ (7.20 g), yttrium nitrate hexahydrate, $Y(NO_3)_3.6H_2O$ (0.372 g), and citric acid (2.90 g) were dissolved in 50 mL of deionized water. The uniform aqueous solution was heated approximately at 230 ˚C with uninterrupted stirring forming the gel. The gel, upon heating, turned into ash. The calcination of ash at 500 ˚C for 4 h in a muffle furnace yielded Y-ZnO nanoparticles. Following the same procedure taking ammonium vanadate, NH_4VO_3 (0.12 g) in place of $Y(NO_3)_3.6H_2O$, V-ZnO nanoparticles were prepared. For Y-V-ZnO nanoparticles, $Y(NO_3)_3.6H_2O$ (0.093 g), and NH_4VO_3 (0.090g) together were taken.

4.1.2.2. Synthesis of PANI-rGO

The synthesis of rGO was achieved by modified Hummer's method [Jaiswal et al. (2016), Verma et al. (2019)]. For grafting conductive polyaniline chains on the rGO nanosheets, *in-situ* oxidative polymerization of aniline was performed using ammonium peroxide sulfate as an oxidizing agent [Amrollahi et al. (2019)]. To accomplish this, 0.50 g of rGO dispersed in 20 mL deionized water was added to an aqueous solution containing 20 mL of 1M HCl, aniline (1 mL), and ammonium peroxide sulfate (0.25 g). The resulting mixture was stirred for 24 h at room temperature when dark green polyaniline (PANI) was

deposited on the rGO nanosheets. After filtration and thorough washing with deionized water, the final product rGO-PANI was obtained.

4.1.2.3. Synthesis of Y-V-ZnO/PANI-rGO

The mixture of Y-V-ZnO nanoparticles (0.5 g) and PANI-rGO (0.5 g) in 30 mL of ethanol was stirred for 2h, followed by 1 h reflux. The product obtained was filtered and dried in a vacuum.

4.2. Sample Preparation

For sample preparation, reduced graphene oxide (rGO), polyaniline (PANI), the composite PANI-rGO, the nanoparticles of ZnO, V-ZnO, Y-ZnO, Y-V-ZnO, and the final composite Y-V ZnO /PANI-rGO were blended with paraffin oil by uninterrupted stirring for 2h at 50^{o}C and further sonicating for 1h at room temperature. The additives provided the tribological activity in different ranges of concentration, accordingly the samples were prepared ; nanoparticles 0.00, 0.05, 0.10, 0.15, 0.20, 0.25, 0.30 %w/v, PANI and rGO 0.00, 0.05, 010, 0.15, 0.20 %w/v PANI- rGO and Y-V ZnO /PANI-rGO 0.00, 0.0025, 0.005, 0.0075, 0.010, 0.0125, 0.015, 0.0175, 0.020 %w/v. Since the maximum antiwear activity was observed at 0.005%w/v of the final composite, this concentration was considered as the optimized concentration for conducting the tribological tests.

The activity was tested for Y-V-ZnO nanoparticles in the range (0-0.30 %w/v) with maximum antiwear efficiency at 0.25 %w/v, **Fig. 4.6a.**

In the case of PANI and rGO, the antiwear activity has been tested in the range (0-0.20 %w/v). As evident in **Fig. 4.6b**, the greatest efficiency is observed at 0.1 and 0.15 %w/v for PANI, and rGO, respectively. Since PANI-rGO performs much better than PANI or rGO, the concentrations (0-0.020 %w/v) were tested for tribological activity, and 0.0125 %w/v was ascertained as the optimized concentration, **Fig. 4.6c.** Finally, Y-V-ZnO/PANI-rGO revealed illustrious activity **(Fig. 4.6 c),** and a very low concentration, 0.005 %w/v, yielded the highest activity. Thus, the optimized concentration for the other tribological tests was contemplated to be 0.005 %w/v.

4.3. Results and Discussion

4.3.1. Characterization of Additives

TEM/HR-TEM and HR-SEM techniques have been employed for morphological studies of the investigated additives. HR-SEM images of rGO, PANI, PANI-rGO, and Y-V-ZnO/PANI-rGO are illustrated in **Fig. 4.1.a(i-iv)**.

Fig. 4.1a(i) displays the layered structure of rGO with a puckered surface and pleated ends [Verma et al. (2019)]. The chains of rod-like PANI are visible in **Fig. 4.1a(ii)**. **Fig. 4.1a(iii)** shows PANI functionalized rGO (PANI-rGO), PANI chains adhered irregularly on the surface of layered rGO can be seen clearly [Amrollahi et al. (2019), Liu et al. (2018)]. The average diameter of rod-like PANI could be obtained between 7 to 9 nm. **Fig. 4.1a(iv)** manifests the nanoparticles anchored on the surface of the PANI-rGO hybrid. The element

mapping of Y-V-ZnO/PANI-rGO, **Fig. 4.1(b)** affirmed a uniform distribution of the elements authenticating the formation of the composite and has been appended as **Fig. 4.1b**.

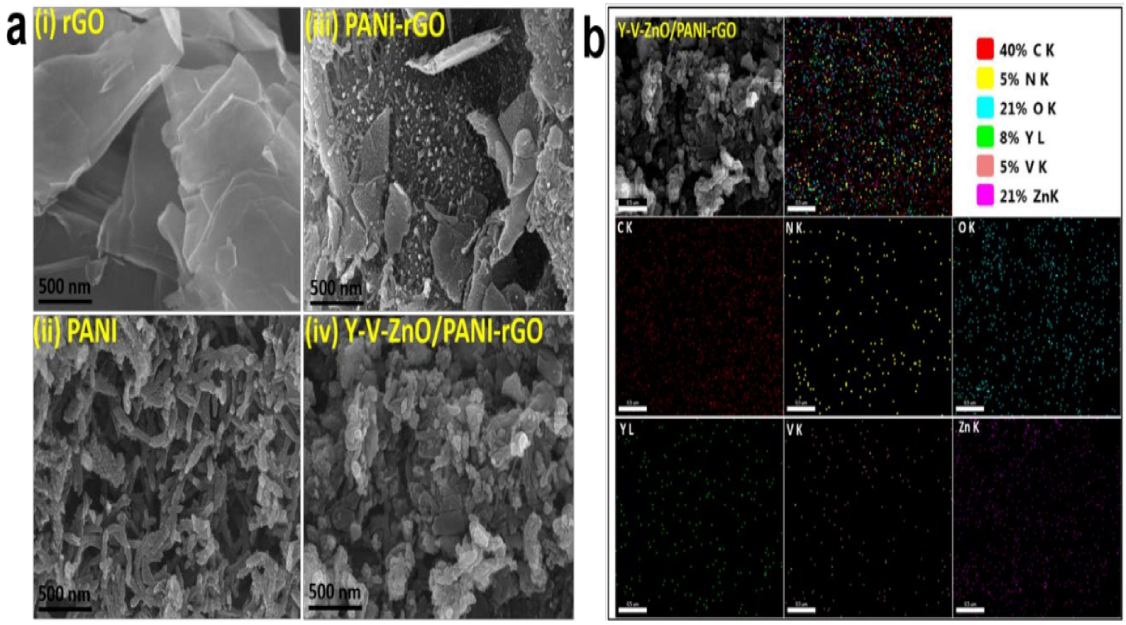

Fig. 4.1. (a) HR-SEM images of (i) rGO, (ii) PANI, (iii) PANI-rGO, (iv) Y-V-ZnO/PANI-rGO and (b) Elemental mapping of Y-V-ZnO/PANI-rGO.

The TEM images of rGO, PANI, PANI-rGO nanosheets, ZnO, Y-V-ZnO nanoparticles, and Y-V-ZnO/PANI-rGO nanocomposite are produced in **Fig. 4.2a**, **4.2b**, **4.2c**, **4.2d**, **4.2e**, and **4.2f**, respectively. The rGO nanosheets with rumpled margins are observable in **Fig. 4.2a**. The rod-like PANI with 7-9 nm width is identified in **Fig. 4.2b**. The functionalization of rGO by PANI is evinced in **Fig. 4.2c.** The TEM image of Y-V-ZnO/PANI-rGO, **Fig. 4.2f** depicts doped nanoparticles garnishing PANI functionalized rGO nanosheets.

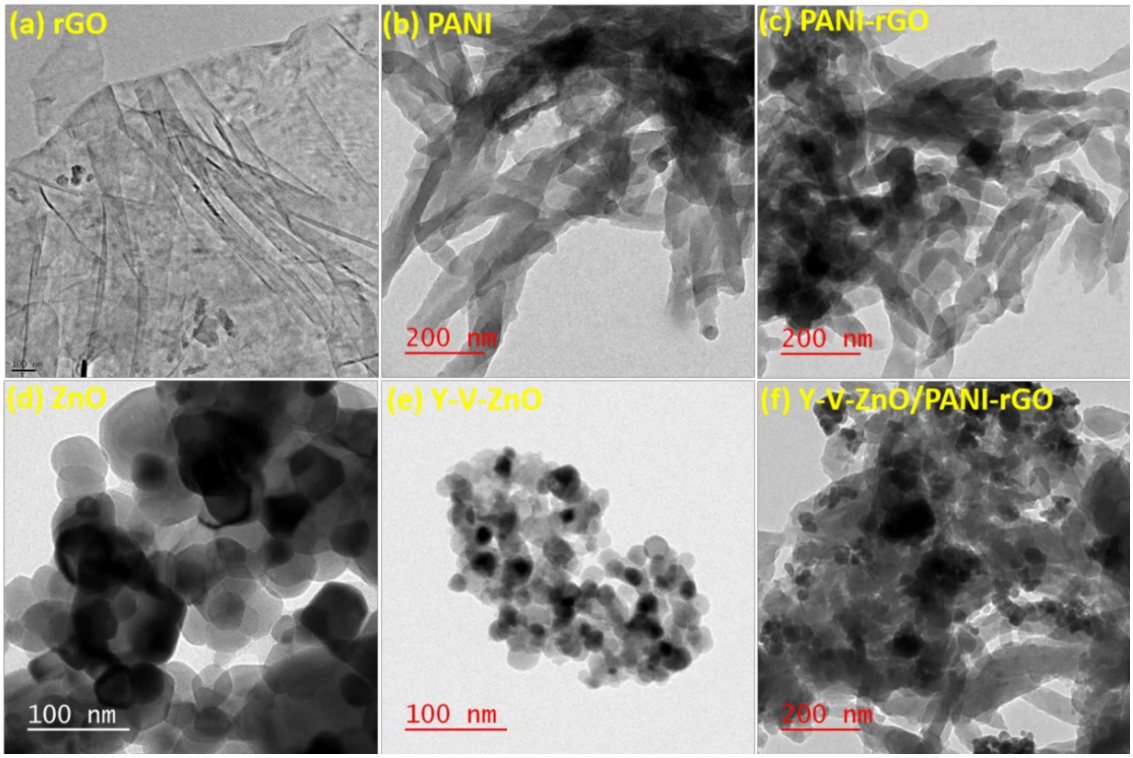

Fig. 4.2. TEM images of (a) rGO, (b) PANI, (c) PANI-rGO, (d) ZnO, (e) Y-V-ZnO, and (f) Y-V-ZnO/PANI-rGO.

Structural elucidation of the additives has been accomplished by powder-XRD and FTIR spectra. XPS studies of Y-V-ZnO/PANI-rGO have also been performed to identify the chemical states of different elements.

Fig. 4.3a portrays the XRD patterns of rGO, PANI, PANI-rGO, Y-ZnO, V-ZnO, Y-V-ZnO, and Y-V-ZnO/PANI-rGO. The presence of a broad peak at 24.5° in the diffraction pattern of rGO corresponding to the (002) plane signifies the formation of rGO. The XRD of PANI is

characterized by the peaks at 18.5°, 20.5°, and 25.6°, according to (011), (020) and, (200) planes, respectively [Mahato et al. (2016)].

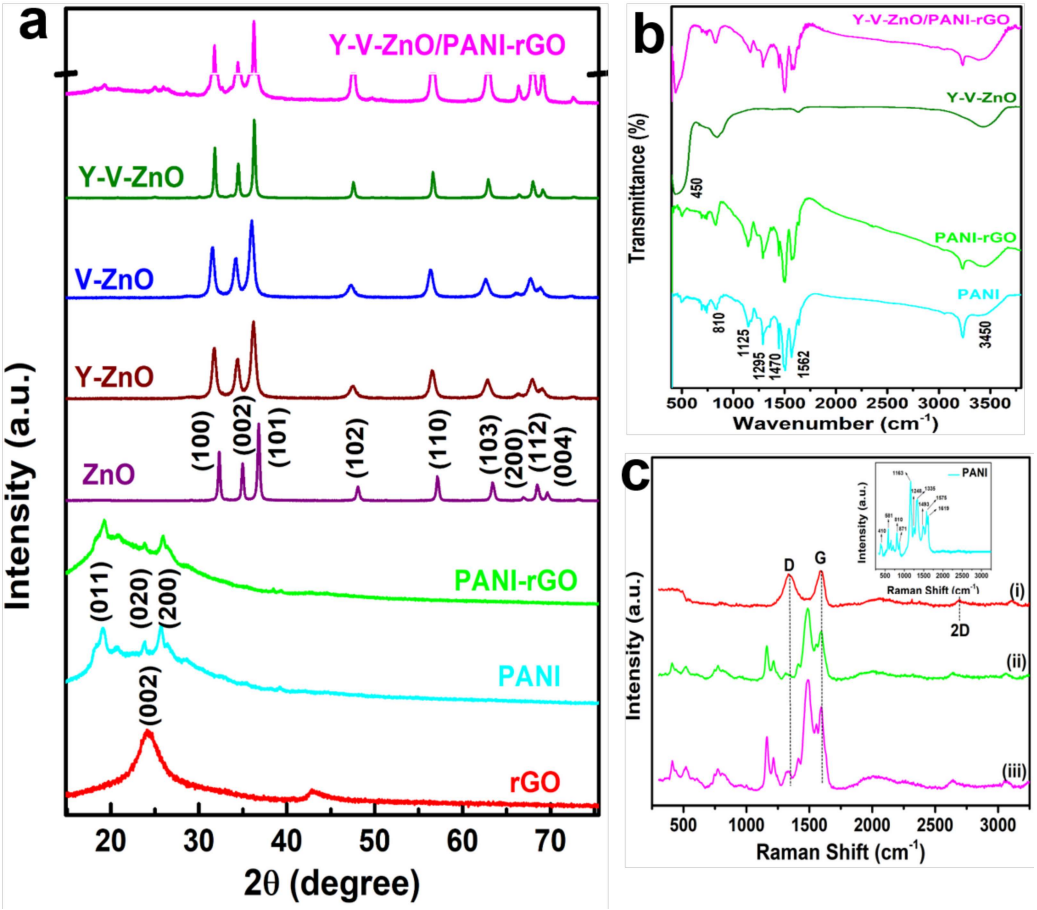

Fig. 4.3. (a) X-ray diffraction (XRD) patterns of as-prepared nanomaterials, (b) FTIR, and (c) Raman spectra of (i) rGO; (ii) PANI-rGO; and (iii) Y-V-ZnO/PANI-rGO nanoadditives (inset showing spectra of PANI).

The composite PANI-rGO exhibits the peaks due to both PANI and rGO together in the region 15-30°. The diffraction patterns of Y-ZnO, V-ZnO, and Y-V-ZnO withhold the hexagonal wurtzite structure of ZnO (JCPDS no. 36-1451) [Verma et al. (2019), Joshi et

al.(2014)]. Doping by yttrium and vanadium has not yielded any extra peak indicating the continuance of the single phase. Besides, the shifting of peaks towards lower theta value confirms the doping of Y and V into ZnO [Joshi et al.(2014), Alam et al. (2017), Liu et al. (2015)]. The intensity of the peaks, however, has slightly reduced. Debye-Scherrer formula has been used to find out the size of nanoparticles. Interestingly, the size of nanoparticles, ZnO, 30 nm, has tremendously reduced to 16 nm for Y-V-ZnO [Alam et al. (2017), Liu et al. (2015)]. The diffraction pattern of the composite, Y-V-ZnO/PANI-rGO, exhibits characteristic peaks of Y-V-ZnO. The peaks due to rGO and PANI have been observed in the region 15-30°.

The FTIR spectra of PANI, PANI-rGO, Y-V-ZnO, and Y-V-ZnO/PANI-rGO are presented in **Fig. 4.3b**. The spectrum of PANI shows a broad peak due to N-H stretching vibration at 3450 cm^{-1} [Verma et al. (2020), Mahato et al. (2016), Liu et al. (2018)]. The peaks centered at 1562 and 1470 cm^{-1} are attributed to C=C stretching vibrations of the quinoid and benzenoid rings, respectively, indicating the emeraldine state of PANI. Besides, the peaks at 1295, 1125, and 810 cm^{-1} are assigned to the C-N stretching and C-H bending in the plane, and out-of-plane vibrations, respectively [Verma et al. (2020), Mahato et al. (2016),]. All the characteristic peaks of PANI and rGO are visible in the spectrum of PANI-rGO. The little shifts in quinoid skeletal vibration of PANI (from 1562 to 1580 cm^{-1}), benzenoid vibration (from 1470 to 1498 cm^{-1}), and C-H in-plane bending (from 1125 to 1142 cm^{-1}) support a substantial interaction between the quinoid ring of PANI and the basal plane of rGO in the composite. In addition to the distinctive peaks due to PANI-rGO, the metal-

oxygen stretching mode of Y-V-ZnO is also identified at 450 cm^{-1} in the spectrum of Y-V-ZnO/ PANI-rGO.

All the characteristic peaks of PANI could be clearly spotted in the Raman spectrum of PANI (**Fig. 4.3c**). The bands at 410, 581, 810, and 871 cm^{-1} are ascribed to out of the plane and in-plane vibration of protonated emeraldine form [Verma et al. (2020), Qin et al. (2017), Yang et al. (2017)]. The C-H bending vibration has been located at 1163 cm^{-1}. The bands at 1248, 1335, 1493 cm^{-1} have been assigned to stretching modes of vibrations of C-N, C-N^{+}, and C=N of the benzenoid ring, respectively [Qin et al. (2017), Yang et al. (2017)]. The C=C stretching modes of benzenoid and quinoid rings could be identified at 1575 and 1619 cm^{-1}, respectively.

Raman spectrum of rGO exhibits two intense peaks at 1360 and 1582 cm^{-1}, assignable to D and G bands, respectively. The G band denotes graphitic form with sp^2- hybridized carbon atoms, while the D band unveils deviations or disorders from the well-ordered graphitic structure. In the composite PANI-rGO, the D band shifts towards lower wavenumber, which indicates strong π-π interactions between PANI and rGO [Qin et al. (2017), Yang et al. (2017)]. The ratio of I_D and I_G of rGO has substantially decreased in PANI-rGO, which signifies that the orderliness has enhanced or defects have declined [Amrollahi et al. (2019), Yang et al. (2017)]. However, further addition of Y-V-ZnO has enhanced the ratio indicating thereby the advancement of defects. All the peaks of PANI could be identified in the composites of PANI-rGO and Y-V-ZnO/PANI-rGO.

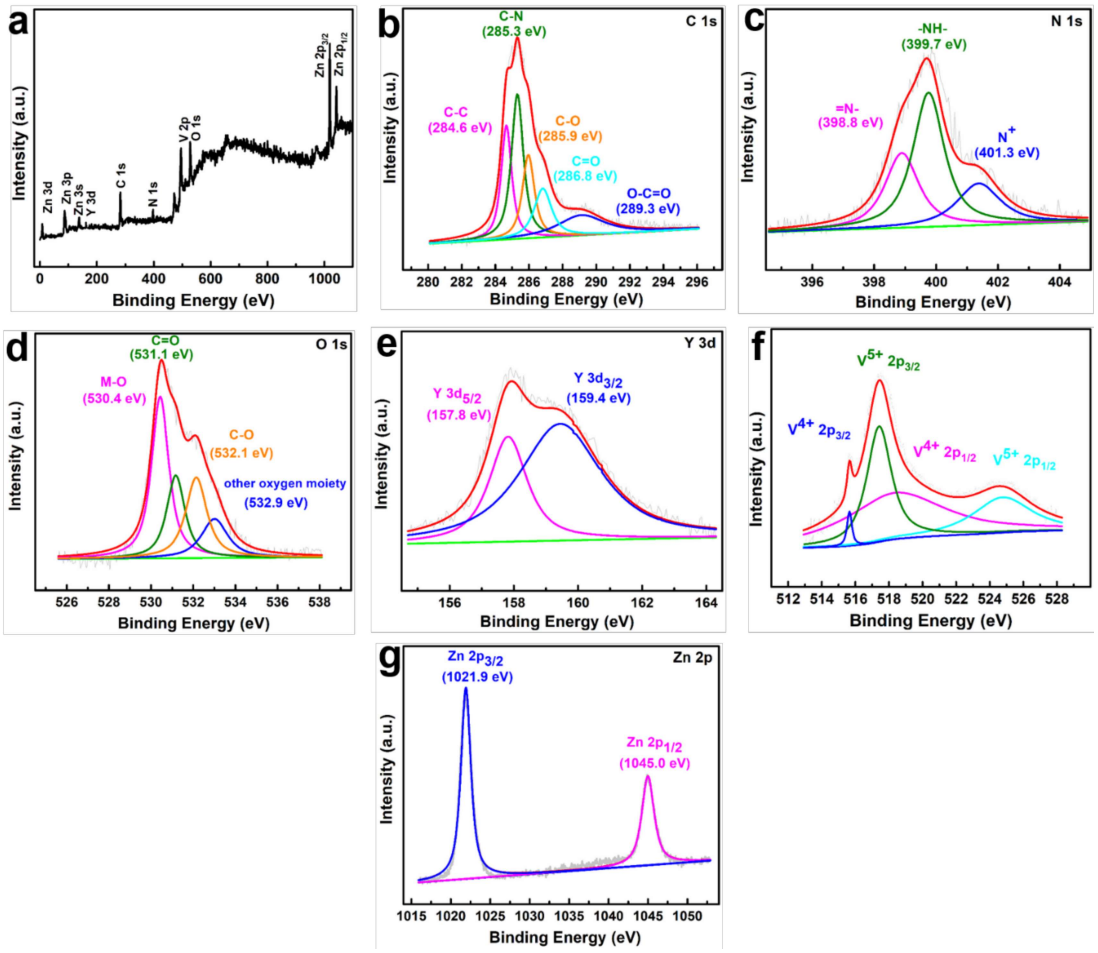

Fig. 4.4. (a) XPS survey spectra and deconvoluted XPS images of Y-V-ZnO/PANI-rGO nanomaterial: (b) C 1s, (c) N 1s, (d) O 1s, (e) Y 3d, (f) V 2p, and (g) Zn 2p.

The presence of carbon, nitrogen, oxygen, yttrium, vanadium, and zinc could be verified by the survey spectrum of Y-V-ZnO/PANI-rGO (**Fig. 4.4a**). The XPS peak software was utilized to find out the chemical states of these elements. The deconvoluted core level spectra of C 1s, N 1s, O 1s, Y 3d, V 2p, and Zn 2p are illustrated in **Fig. 4.4(b-g)**. The XPS peaks of C 1s (**Fig. 4.4b**) are further decomposed into five Gaussian peaks with binding energies

284.6, 285.3, 285.9, 286.8, and 289.3 eV, which could be allocated to C-C/C=C, C-N, C-O, C=O, and O-C=O bonds, respectively [Yang et al. (2017), Qin et al. (2017), Han et al. (2014), Verma et al. (2019)]. The XPS peaks of N 1s (**Fig.4.4 c**) conform to the presence of quinoid amine groups (=N-), the benzenoid amine nitrogen (-NH-), and cationic nitrogen (N^+) with binding energies 398.8, 399.7, and 401.3 eV, respectively [Yang et al. (2017), Han et al. (2014), Qin et al. (2017)].

The O 1s spectrum **Fig. 4.4d** shows peaks, with binding energies, 530.8 and 531.1 eV assignable to >C=O, and C-OH bonds of rGO, respectively [Verma et al. (2019), Yang et al. (2017), Qin et al. (2017)]. The peak around binding energy, 530.3 eV, is ascribed to the oxide ions in the metal oxide [Liu et al. i. (2015), Verma et al. (2019), Alam et al. (2017). Besides, a peak at 532.9eV corresponds to the other oxygen moieties or adsorbed water molecules [Liu et al. (2015), Yang et al. (2017)]. Furthermore, the C=O peak observed at 532.32 eV in rGO has shifted to 531.1 eV in the case of rGO/PANI [Qin et al. (2017)]. The shift in the peak indicates the increase in electron density at oxygen atoms after interaction with PANI **(Fig.4.4d) [**Qin et al. (2017)].

The appearance of two peaks centered at 159.4 and 157.8 eV in the spectrum of Y 3d (**Fig. 4.4e**) could be attributed to the binding energy of Y $3d_{3/2}$ and $3d_{5/2}$, respectively [Shukla et al. (2020), Alam et al. (2017)]. Further, XPS spectrum of V 2p exhibits V^{5+} $2p_{3/2}$ and V^{4+} $2p_{3/2}$ at binding energies 517.3 and 515.7 eV, respectively (**Fig. 4.4f**). The V^{5+} $2p_{1/2}$,

and V^{4+} $2p_{1/2}$ species are observed at 524.5 and 522.1eV, respectively [Silversmit et al. (2004)]. Thus, XPS studies verify the fruitful doping of V and Y ions together in ZnO.

The spectrum of Zn $2p_{3/2}$ is characterized by the peaks at 1021.9 eV and 1045 eV corresponding to Zn $2p_{3/2}$ and Zn $2p_{1/2}$, respectively (**Fig. 4.4g**), which validates the formation of hexagonal ZnO [Verma et al. (2019), Alam et al. (2017)].

4.3.2. Dispersion Stability of Nanoadditives

The dispersion stability of the investigated formulations was studied by UV/visible spectroscopy. The absorbance values were noted in the range of 200-800 nm after every 12 h up to 72 h. The test samples were prepared by ten-fold dilution of the optimized concentration (0.005%w/v) using PO.

The spectrum of Y-V-ZnO/PANI-rGO, inset **Fig.4.5a,** exhibits the bands of the components. ZnO absorbs at 386 nm due to wide bandgap [Alam et al. (2017), which is blue-shifted in the doped zinc oxide, Y-V-ZnO [Mitra et al. (2015), Alam et al. (2017)]. The absorption band of rGO is visible at 276 nm for π-π* transition whereas bands of PANI are observed in the range of 300-500nm corresponding to π-π* transition in the benzenoid ring, polaron-π*(where benzenoid or quinoid) and exciton formation in the quinoid rings, the bands of PANI have shifted towards a higher wavelength in the composite. The shifting of the bands recommends the formation of a charge-transfer complex between PANI and rGO [Amrollahi et al. (2019), Mitra et al. (2015)].

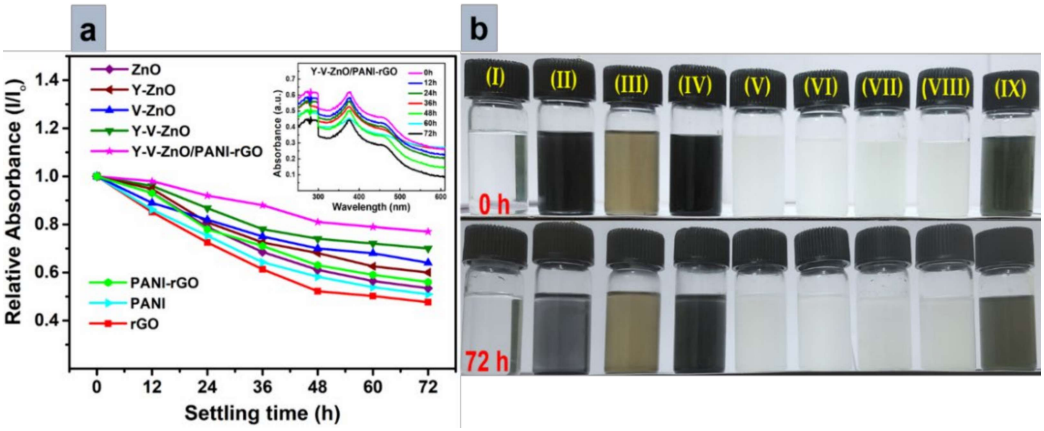

Figure 4.5. (a) Dispersion stabilities of base oil containing rGO, PANI, PANI-rGO, ZnO, Y-ZnO, V-ZnO, Y-V-ZnO, and Y-V-ZnO/ PANI-rGO studied by UV-vis spectrophotometry **(b)** Optical photographs of (I) plain PO, and PO with dispersed nano additives (II) rGO, (III) PANI, (IV) PANI-rGO, (V) ZnO, (VI) Y-ZnO, (VII) V-ZnO, (VIII) Y-V-ZnO, and (IX) Y-V-ZnO/ PANI-rGO at zero time and after 72 hours.

The absorbance values of Y-V-ZnO/PANI-rGO in the range 200-800 nm from zero to 72 h at 12 h intervals are also shown in the Figure. **Fig. 4.5a** illustrates the variation of relative absorbance as a function of settling time for different additives. According to the relative absorbance shown in Figure, additives are supposed to possess ample stability. The stability of PANI-rGO has boomed after the involvement of nanoparticles. **Fig. 4.5b** displays photographs of blends of all the additives in PO initially and after every 12h interval up to 72h showing minimum settling in the case of Y-V-ZnO/PANI-rGO.

4.3.3. Evaluation of Tribological Properties

For the optimization of concentrations of different additives, antiwear tests were conducted following ASTM D4172 test conditions. Surprisingly, all the additives have shown widely

different ranges of concentrations for their antiwear activity. For Y-V-ZnO nanoparticles, the activity was tested in the range (0-0.3 %w/v) with maximum antiwear efficiency at 0.25%w/v, **Fig. 4.6a.** In the case of PANI and rGO, the antiwear activity has been tested in the range (0-0.20 %w/v). As evident in **Fig. 4.6b**, the greatest efficiency is observed at 0.1 and 0.15 %w/v for PANI, and rGO, respectively. Since PANI-rGO performs much better than PANI or rGO, the concentrations (0-0.020 %w/v) were tested for tribological activity, and 0.0125 %w/v was ascertained as the optimized concentration, **Fig. 4.6c.** Finally, Y-V-ZnO/PANI-rGO revealed illustrious activity **(Fig. 4.6 c),** and a very low concentration, 0.005 %w/v, yielded the highest activity. Thus, the optimized concentration for the other tribological tests was contemplated to be 0.005 %w/v.

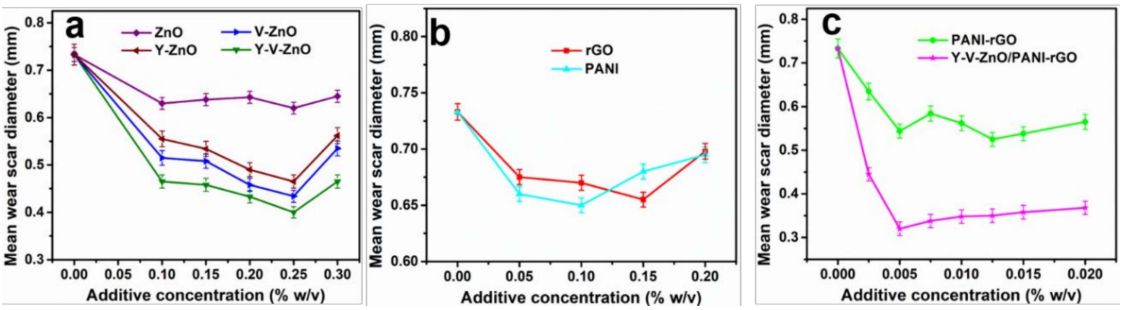

Fig. 4.6. Optimization of the concentration of nano additives in paraffin oil.

The test for the decrement in the wear of base lube containing the investigated additives was conducted at the optimized concentration 0.005% w/v according to ASTM D4172 norms; load 392 N, time 60 min, sliding speed 1200 rpm; temperature, 75 °C.

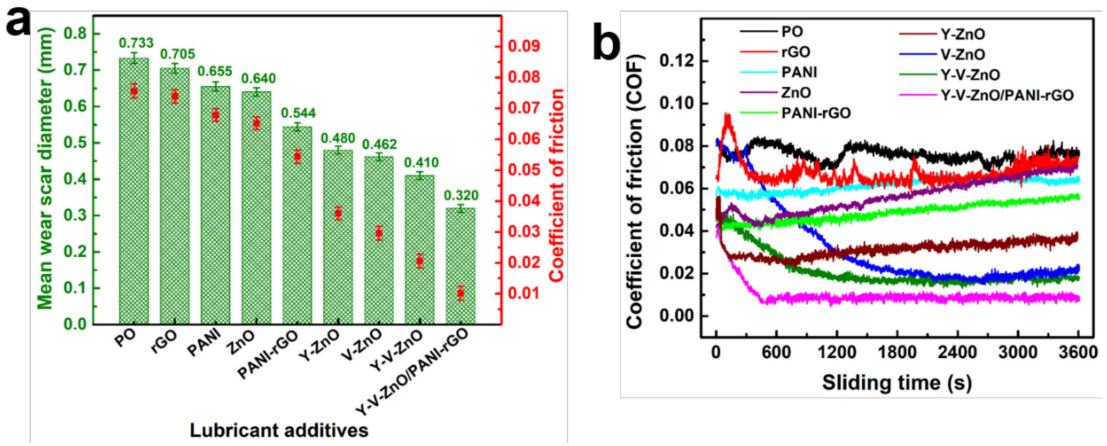

Fig. 4.7. (a) Variation in tribological parameters in the absence and presence of different nano additives (0.005% w/v) in paraffin oil: load, 392 N; sliding speed, 1200 rpm; temperature, 75 °C; sliding duration, 60 min; concentration of additives, 0.005% w/v. **(a)** MWD and the average COF **(b)** COF as a function of sliding time.

The bar diagram, **Fig. 4.7a,** manifests the accumulated experimental data for mean wear scar diameter (MWD) and the average coefficient of friction (COF) concurrently. The MWD for the plain paraffin oil (0.733) reveals perceivable slackening in the presence of its admixtures with; rGO (3.8%), PANI (10.6%), ZnO (12.7%), PANI functionalized rGO (25.8%), yttrium-doped ZnO (34.5%), vanadium-doped ZnO (37%), yttrium-vanadium co-doped zinc oxide (44%), and finally the composite yttrium-vanadium co-doped ZnO with PANI functionalized rGO (56.3%). Likewise, COF data show advancement in % reduction for blends with the tested additives; rGO (8.3%), PANI (14.3%), ZnO (24.3%), PANI-rGO (30.7%), Y-ZnO (55%), V-ZnO (64.5%), Y-V-ZnO (75%), and Y-V-ZnO/PANI-rGO (88.5%). Thus, the maximum antiwear and antifriction efficiencies are perceptible with the composite Y-V-ZnO/PANI-rGO, accentuating synergistic interaction between the components.

Fig. 4.7b divulges the variation of COF of adjacent surfaces as a function of time at 392 N load in the base lube and the formulations containing additives. The COF values for all the formulations keep in countenance with the antiwear efficiency. The extremely low COF-value of COF 0.0087 observed for the composite Y-V-ZnO/PANI-rGO accounts for a strong, tenacious tribofilm giving superlubricity [Wang et al. (2020)].

For wear rate determination, mean wear volume (MWV)is considered to be more significant than MWD. At first, the antiwear test was carried out at 392 N for 1.5 h. After every 15 min, the MWD values were noted. From the observed MWD values, corresponding values of MWV were calculated. MWV versus sliding time graph was plotted and presented in **Fig. 4.8**. The wear rate was obtained by fitting a linear regression model [Jaiswal. et al. (2016), Verma et al. (2019)]. According to the nature of the graph, the span up to 0.75 h was contemplated as running-in followed by steady-state. The running-in and steady-state wear rates were calculated correspondingly and are collected in **Table 4.1**. It is noteworthy that functionalization of rGO with PANI and Y-V-ZnO has resulted in the improvement of reduction in running-in wear rate by 88% and that of steady-state wear rate by 96%. A comparison from plain paraffin oil shows a 94% reduction in running-in wear rate and 98% in steady-state wear rate. **Fig. 4.9** and **Fig. 4.10** display running -in and steady-state wear rates. The wear rates conform with the antiwear efficiencies of the additives.

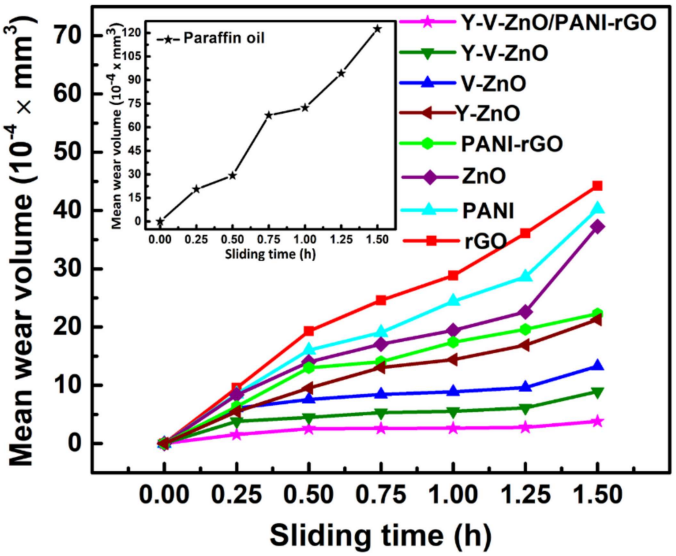

Fig. 4.8. Variation of MWV with the sliding time for a 1.5 h test duration

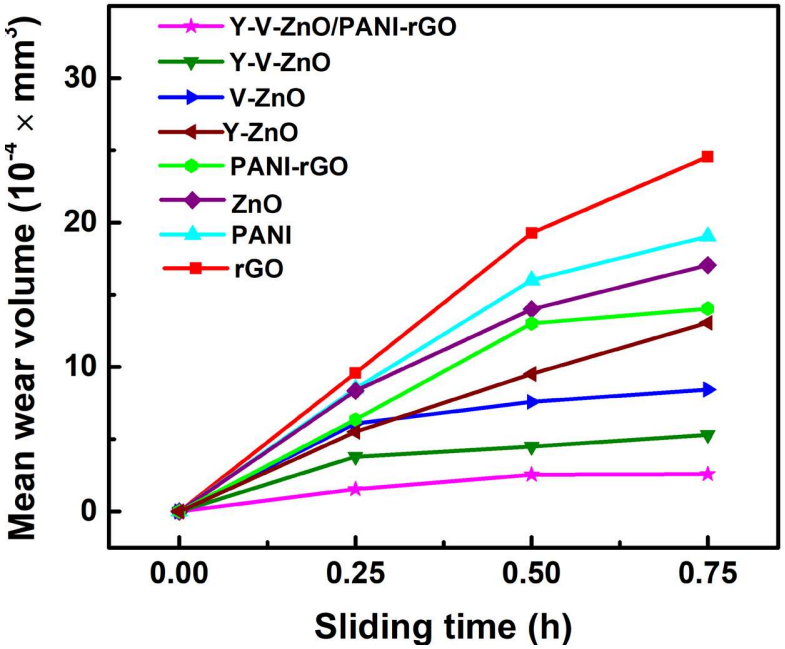

Fig. 4.9. Determination of running-in wear rate by varying mean wear volume with time (h) for paraffin oil containing (0.005% w/v) nano additives at 392 N applied load

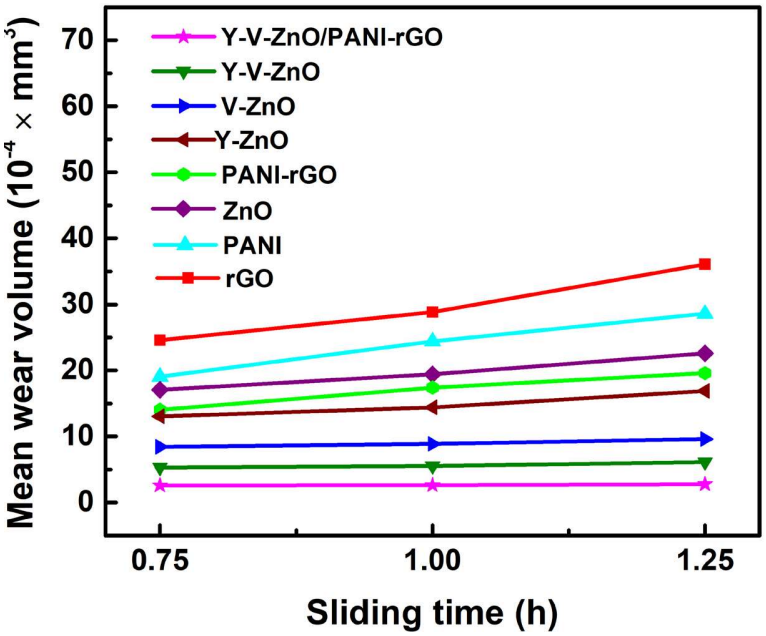

Fig. 4.10. Determination of steady-state wear rate by varying mean wear volume with time (h) for paraffin oil containing (0.005% w/v) nano additives at 392 N applied load.

Table 4.1. Wear-rate for paraffin oil (PO) in the presence and absence of nano additives for 60 min test duration at 392 N applied load

no.	lubricants	wear rate (10^{-4} × mm^3/h)	
		running-in	steady-state
1	PO	84	53
2	rGO	42	25
3	PANI	30	14
4	ZnO	22	12
5	PANI-rGO	18	8
6	Y-ZnO	14	6
7	V-ZnO	10	5
8	Y-V-ZnO	7	2
9	Y-V-ZnO/PANI-rGO	5	1

The base lube, in the absence of any studied additives, exhibits very high running-in and steady-state wear rates. However, in the presence of the additives, significant slackening is observed in the wear rates. The immensity of reduction in wear rates authenticates the antiwear efficiencies of the formulations. There is comparatively higher friction during the running-in period as surface irregularities are to be customized; therefore, the wear rate is high. Conversely, friction is least around the steady-state since the surfaces become accustomed, and the wear rate is significantly reduced. The least possible steady-state wear rate helps in prolonging the life span of the interacting surfaces. It is important to note that in the case of the composite Y-V-ZnO/rGO-PANI, the steady-state wear rate is too low, implying its illustrious antiwear efficiency.

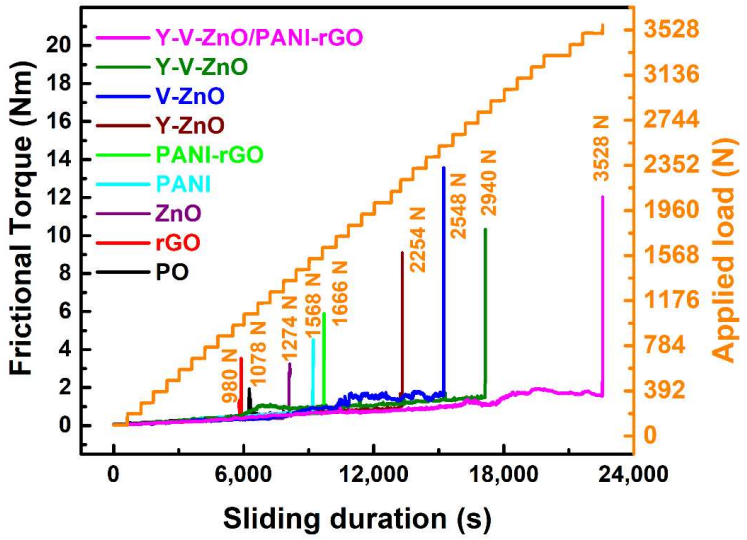

Fig. 4.11. Variation of frictional torque as a function of stepwise loading and time for different nano additives: sliding speed, 600 rpm; temperature, 75 °C; concentration of additives, 0.005% w/v.

The step loading test was performed according to ASTM D5183 conditions; 392 N load, 600 rpm, 75°C temperature, 60 min using 0.005% w/v concentration of the additives. The test was further continued by appending 98 N load after every 10 min, and the corresponding values of the frictional torque were noted. The deviation of frictional torque as a function of the applied load is depicted in **Fig. 4.11**. The observed seizure load at which the tribo-surfaces are seized is considered as a measure of the load-bearing capacity of the investigated additives. In the absence of the additives, the plain oil shows seizure load at 1078 N. Improvement in load-bearing capacity is obtained when additives are blended with the oil; ZnO (1274 N), PANI (1568N), PANI-rGO (1666 N), Y-ZnO (2254 N), V-ZnO (2548 N), Y-V-ZnO (2940 N), and Y-V-ZnO/rGO-PANI (3528 N). The rGO appears to be an exception, which even reduces it to 980N because of its poor adsorption over the surface. It may be inferred that in the case of Y-V-ZnO/rGO-PANI strength of the developed tribofilm is adequately high to bear such a high load.

4.3.4. Morphology of the Wear Track

The SEM and AFM techniques were applied to investigate the distinctive morphological features of the wear scar surface after ASTM D4172 test. As apparent in **Fig. 4.12**, the SEM image of paraffin oil without any additive exhibits a tremendously crinkled surface with MWD 0.733 mm. Conversely, the wear scar surface is quite even in the presence of different formulations.

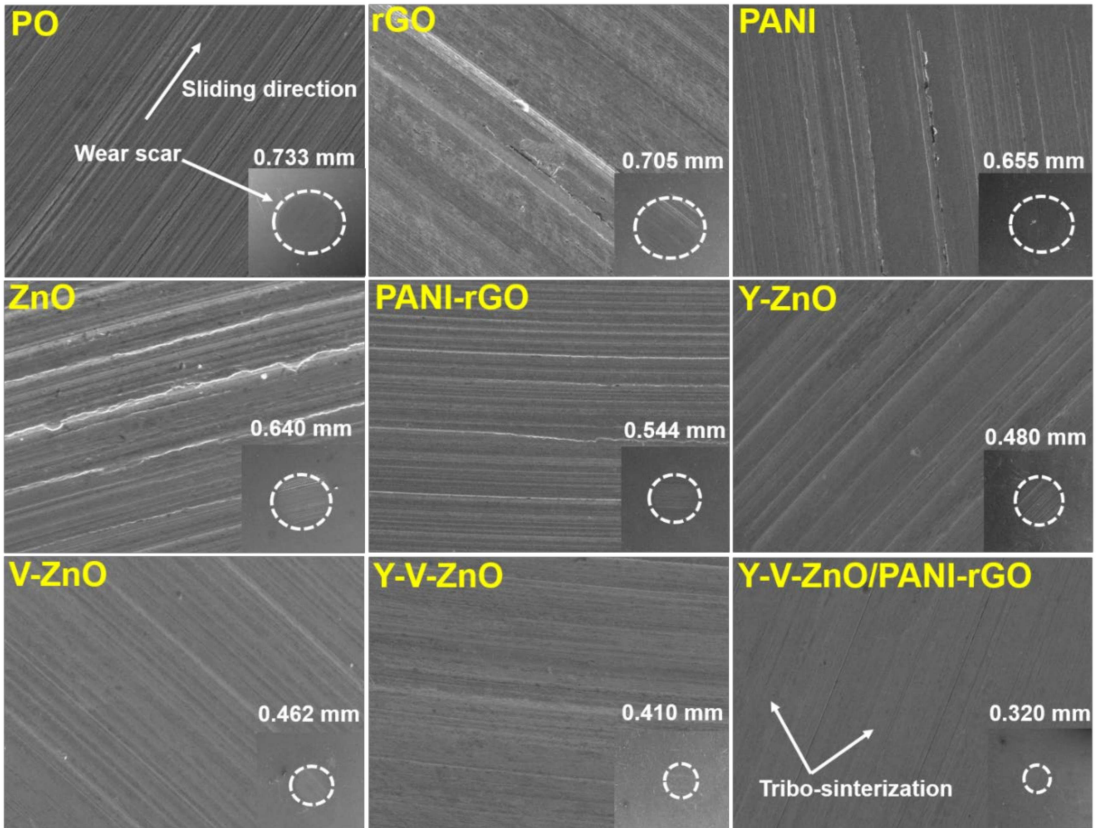

Fig. 4.12 SEM micrographs (inset: full view of the wear scar at 100× and wear scar surface at 2.00K× magnification) of the worn steel surface lubricated with PO with and without different nano additives [0.005% (w/v)] after the antiwear test

The magnitude of evenness of the surfaces may be correlated with the antiwear properties of the studied additives. The MWD values for all the formulations are incorporated in the inset of all the micrographs; rGO (0.705mm), PANI (0.655mm), ZnO (0.640mm), PANI functionalized rGO (0.544mm), Y-ZnO (0.480mm), V-ZnO (0.462mm), Y-V-ZnO (0.410mm), and at last the composite Y-V-ZnO with PANI-rGO (0.320mm). The extent of

reduction in MWD validates the antiwear efficiencies satisfactorily. Thus, maximum antiwear efficiency is obtained for Y-V-ZnO/PANI-rGO.

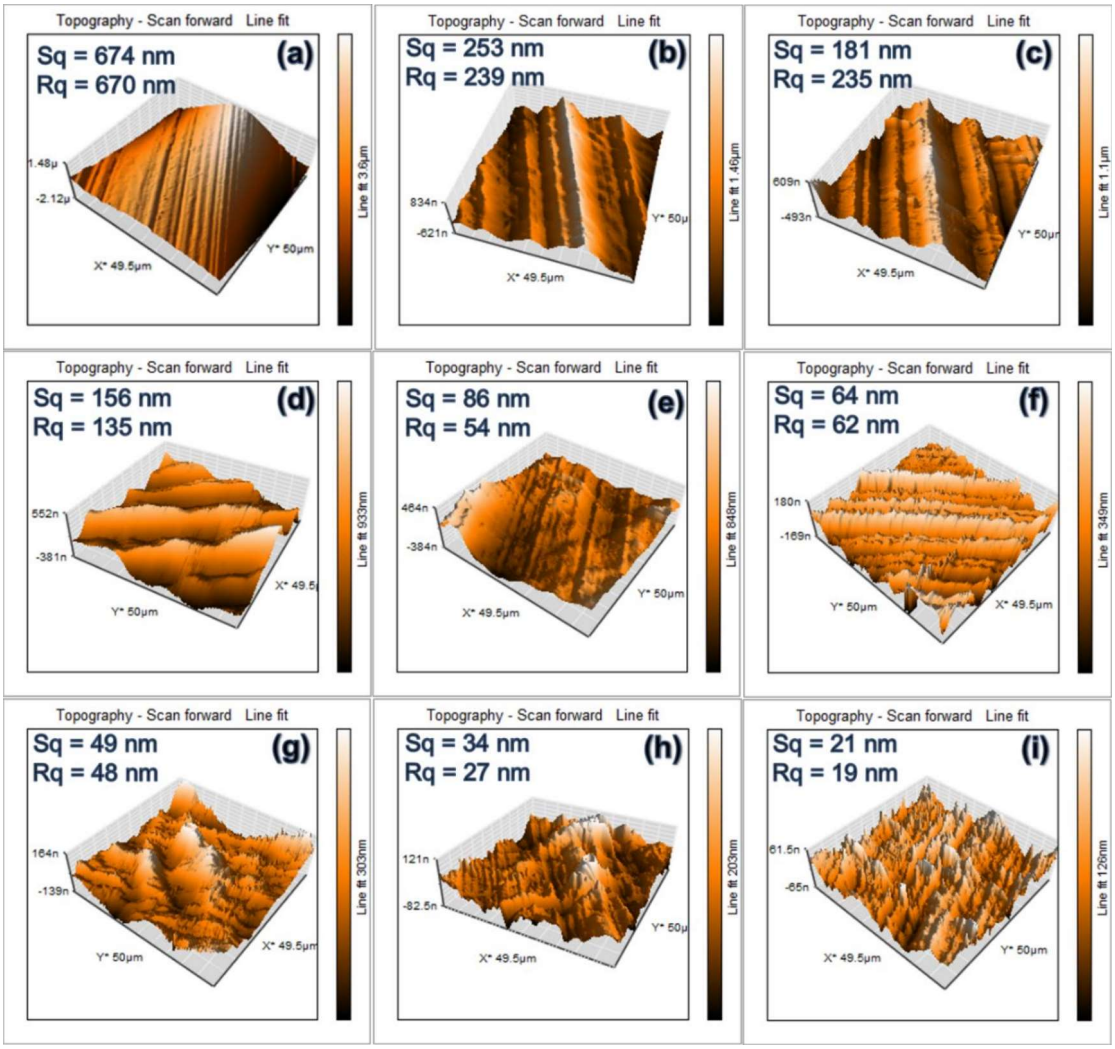

Fig. 4.13. Three-dimensional AFM images of the worn steel surface lubricated with different additives [0.05% (w/v)] in PO after the antiwear test: (a) PO; (b) rGO; (c) PANI; (d) ZnO; (e) PANI-rGO; (f) Y-ZnO; (f) V-ZnO; (g) V-ZnO; (h) Y-V-ZnO; (i) Y-V-ZnO/PANI-rGO.

Fig. 4.13 illustrates the AFM images (*3D)* of the wear scar surface after the antiwear test of plain base oil and oil blended with the investigated additives. The area (Sq) and line roughness (Rq) values are mentioned with all AFM images. The decrease in surface roughness values follows exactly the wear and friction-reducing characteristics of the additives. Needless to say, minimum surface roughness is obtained in the case of Y-V-ZnO/ PANI-rGO.

4.3.5. Characterization of Tribofilm

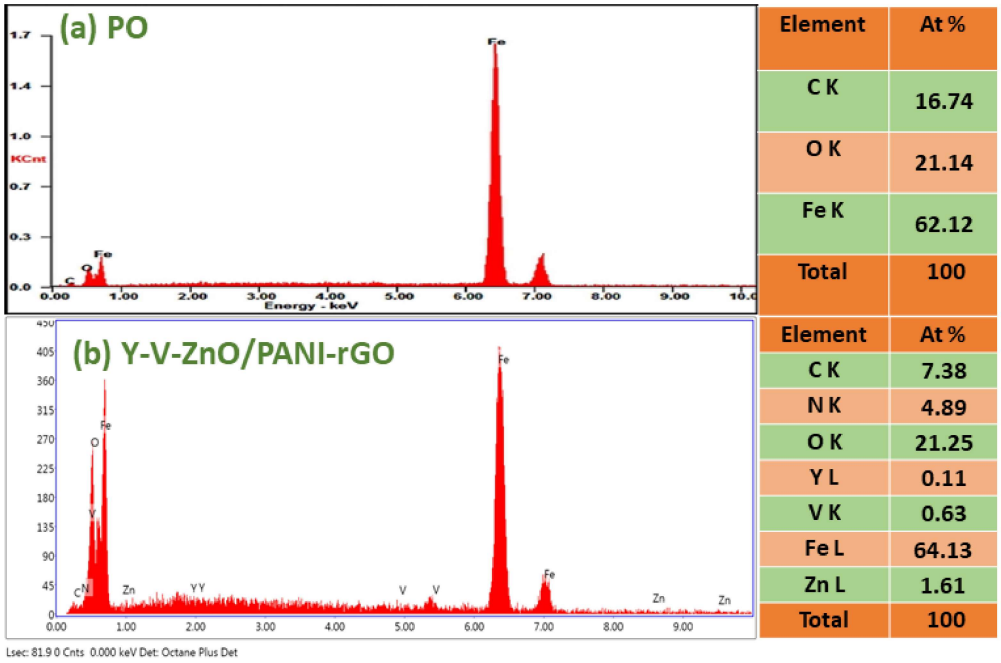

Element	At %
C K	16.74
O K	21.14
Fe K	62.12
Total	100

Element	At %
C K	7.38
N K	4.89
O K	21.25
Y L	0.11
V K	0.63
Fe L	64.13
Zn L	1.61
Total	100

Fig. 4.14. EDX spectra of worn surface lubricated with (a) Blank Paraffin oil (PO) and (b) PO blended with 0.005% w/v Y-V-ZnO/PANI-rGO nanohybrid at 392 N applied load.

The EDX spectrum of the wear scar surface after antiwear test using Y-V-ZnO/PANI-rGO blended with paraffin oil is shown in **Fig. 4.14**; the presence of the elements yttrium, vanadium, zinc along with iron, carbon, oxygen, and nitrogen confirms the adsorption of the additive on the steel surface. All of these elements have cooperated in the invigoration of the tribofilm.

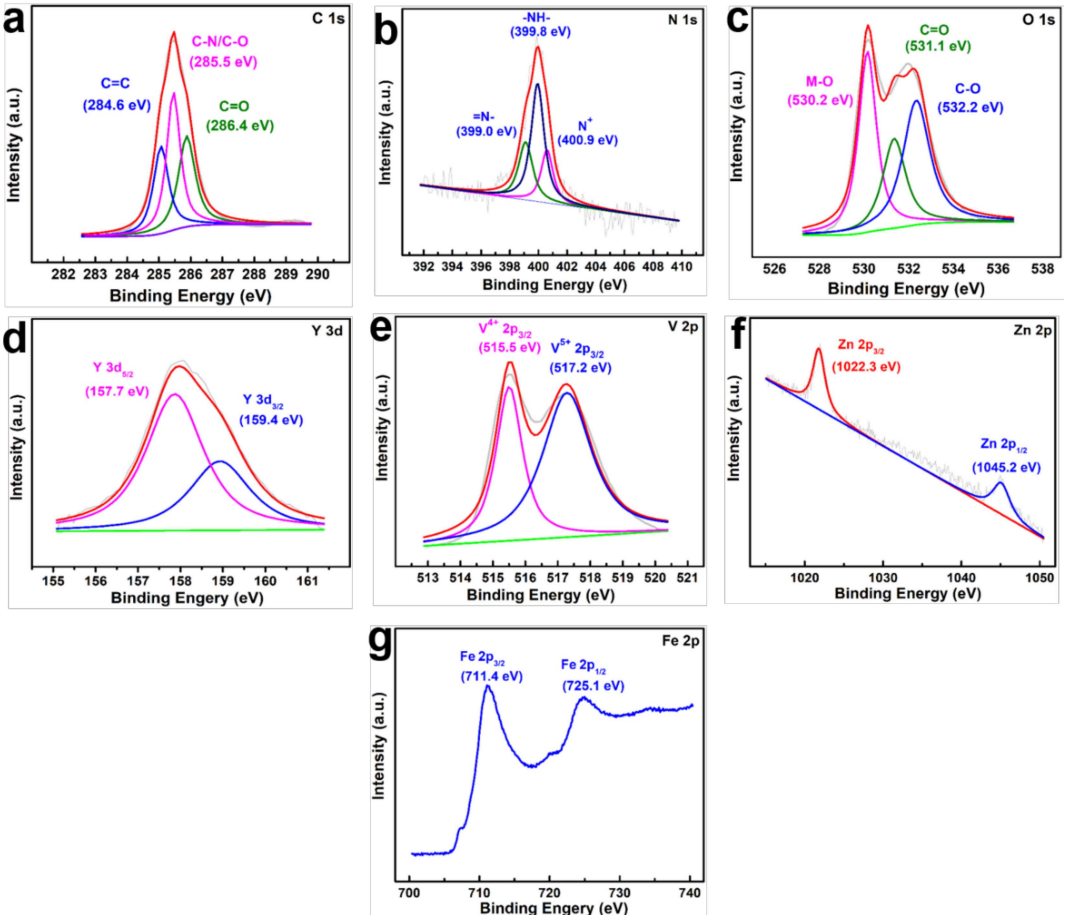

Fig. 4.15. XPS spectra of the worn surface lubricated with the Y-V-ZnO/PANI-rGO nanocomposite: (a) C 1s, (b) N 1s, (c) O 1s, (d) Y 3d, (e) V 2p, (f) Zn 2p and (g) F 2p.

XPS spectra of the wear scar surface in the presence of the ternary composite Y-V-ZnO/PANI-rGO were recorded to find out the chemical states of the constituent elements. The core-level spectra of C 1s, N 1s, O 1s, Y 3d, V 2p, Zn 2p, Fe 2p were deconvoluted using XPS peak-fit software and are displayed in **Fig. 4.15(a-g)**. The XPS peaks of C 1s (**Fig. 4.15a**) could be deconvoluted into five peaks with binding energies 284.6, 285.5, and 286.8 eV, corresponding to C-C/C=C, C-N/C-O, and C=O bonds, respectively [Yang et al. (2017), Qin et al. (2017), Han et al. (2014), Verma et al. (2019)]. The N 1s (**Fig. 4.15b**) peaks with binding energies 399, 399.8, and 400.9 eV, could be accorded with quinoid amine groups (=N-), the benzenoid amine nitrogen (-NH-), and cationic nitrogen (N^+), respectively [Yang et al. (2017), Han et al. (2014), Qin et al. (2017)].

In the O 1s spectrum, **Fig. 4.15c**., the peaks with binding energies, 531.1 and 532.2 eV are ascribed to >C=O, and C-O bonds of rGO, respectively [Verma et al. (2019), Yang et al. (2017), Qin et al. (2017)]. A peak centred at 530.2 eV corresponds to M-O bond (M = Fe/ Zn/ Y/ V) [Verma et al (2019), Shukla et al. (2020)].

XPS spectrum of Y 3d (**Fig. 4.15d**) is characterized by the presence of two peaks at 159.4 and 157.7 eV for Y 3d $_{3/2}$ and 3d $_{5/2}$, respectively, while that of V 2p exhibits V^{5+} $2p_{3/2}$, and V^{4+} $2p_{3/2}$, at binding energies 517.2 and 515.5 eV, respectively (**Fig. 4.15e**)[Silversmit et al. (2004)]. In the Zn 2p spectrum Zn $2p_{3/2}$ and Zn $2p_{1/2}$ are identified at 1022.3 and 1045.2 eV [Verma et al. (2019)].The peaks centered at 711.4 and 725.1 eV in the Fe 2p spectrum for Fe $2p_{3/2}$ and Fe $2p_{1/2}$, respectively [**Fig. 4.15g**], demonstrate the formation of Fe_2O_3 [Verma et al (2019), Shukla et al. (2020)].

4.3.6. Mechanism of Tribo-Interaction of Additives

For tribological activity, additives are at first adhered tenaciously on the tribo surfaces, eventually forming tribofilm under the prevailing conditions of the test. Apparently, the tribofilm bears the applied load. The characteristics of the tribofilm are, indeed, authoritative for comparing the activity of different additives. The poor tribological activity of rGO has been advanced by its functionalization with polyaniline in emeraldine state (PANI-rGO) involving the formation of a charge-transfer complex between aniline (electron donor) and rGO (electron acceptor), achieving an ordered structure [Mahto et al. (2016), Verma et al. (2020)] Besides, electrostatic interactions and hydrogen bonding also exist between PANI and rGO. The advancement in activity may be ascribed to nanorod morphology of PANI owing to its rolling and sliding effects between the tribo surfaces [Verma et al. (2019, 2020), Shukla et al. (2020), Liu et al. (2017)].

Further, anchored yttrium and vanadium co-doped zinc oxide nanoparticles have elevated the activity of the nanohybrid (Y-V-ZnO/PANI-rGO) to superlubricity level. The nanoparticles gracing the functionalized nanosheets have assisted in their separation and succeeded in fending off their re-piling and agglomeration. They have also contributed to enhancing the dispersibility. Nanosheets and nanoparticles have controlled agglomeration of each other. Doping of ZnO by yttrium and vanadium in different oxidation states has increased the activity of nanohybrid due to the introduction of more defects. The nanoparticles might have facilitated lubrication by nano bearing effect. The nanoparticles and nanorods, both

morphologies, have enhanced lubricity by mending the contact surfaces or polishing the abraded surface.

The oxides of vanadium, yttrium, zinc, iron, and the adsorbed products of rGO and PANI constitute the tribofilm. To explain the superlubricity of Y-V-ZnO/PANI-rGO, a possibility of intermetallic alloy formation between yttrium, vanadium, and metal components of steel may be proposed, as revealed by Wei et al. (2017) using Raman spectral studies of the tribofilm. However, it was beyond the scope of the present investigation.

4.4. Conclusions

The nanoparticles were prepared by the auto-combustion method. The composite PANI-rGO was obtained by grafting conductive polyaniline chains using *in situ* oxidative polymerization on rGO nanosheets. Finally, Y-V-ZnO/PANI-rGO was prepared by refluxing ethanolic dispersions of Y-V-ZnO nanoparticles and the composite PANI-rGO. The XRD, along with spectroscopic techniques, FT-IR and Raman were applied to characterize the additives. XPS of the additive Y-V-ZnO/PANI-rGO was also recorded. FE-SEM, TEM, and HR-TEM were used to study morphological features of the additives. The tribological tests ASTM D4172 and ASTM D5183 were conducted to evaluate the tribological activity of the additives. PANI-rGO performed much better than rGO because of the charge transfer complex, but exalted activity was observed after the addition of Y-V-ZnO nanoparticles. The composite Y-V-ZnO/PANI-rGO has shown superlubricity.